

See discussions, stats, and author profiles for this publication at: <https://www.researchgate.net/publication/263945471>

Effects of Catalyst Bed Failure on Thermochemical Phenomena for a Hydrazine Monopropellant Thruster Using Ir/Al₂O₃ Catalysts

ARTICLE in INDUSTRIAL & ENGINEERING CHEMISTRY RESEARCH · APRIL 2012

Impact Factor: 2.59 · DOI: 10.1021/ie202347f

CITATIONS

2

READS

82

6 AUTHORS, INCLUDING:



Seung Wook Baek

Korea Advanced Institute of Science and Tech...

238 PUBLICATIONS 1,999 CITATIONS

SEE PROFILE



Cho Young Han

Korea Aerospace Research Institute

34 PUBLICATIONS 207 CITATIONS

SEE PROFILE



Su Kyum Kim

Korea Aerospace Research Institute

18 PUBLICATIONS 39 CITATIONS

SEE PROFILE



Myoung Jong Yu

Korea Aerospace Research Institute

24 PUBLICATIONS 169 CITATIONS

SEE PROFILE

Effects of Catalyst Bed Failure on Thermochemical Phenomena for a Hydrazine Monopropellant Thruster Using Ir/Al₂O₃ Catalysts

Chang Hwan Hwang,[†] Sung Nam Lee,[‡] Seung Wook Baek,^{*,†} Cho Young Han,[§] Su Kyum Kim,[§] and Myoung Jong Yu[∇]

[†]Propulsion and Combustion Laboratory, School of Mechanical, Aerospace and Systems Engineering, Korea Advanced Institute of Science and Technology (KAIST), 373-1 Guseong-dong, Yuseong-gu, Daejeon 305-701, Republic of Korea

[‡]Nuclear Hydrogen Development and Demonstration, Korea Atomic Energy Research Institute (KAERI), 989-111 Daedeok-daero, Yuseong-gu, Daejeon 305-353, Republic of Korea

[§]Satellite Thermal & Propulsion Team Satellite BUS Division, Satellite Technology Research Laboratory, Korea Aerospace Research Institute (KARI), 169-84 Gwahangno, Yuseong-gu, Daejeon 305-333, Republic of Korea

[∇]Satellite Test Division, Satellite Technology Research Laboratory, Korea Aerospace Research Institute (KARI), 169-84 Gwahangno, Yuseong-gu, Daejeon 305-333, Republic of Korea

ABSTRACT: Hydrazine monopropellant has been used in thrusters for maneuvering satellites and landing spacecraft. Testing and handling procedures for hydrazine monopropellant thrusters are complicated, because of the toxicity of the hydrazine and its decomposition product gases. Therefore, simulated numerical analysis can help elucidate the effects of various thruster design parameters and can reduce both development time and expenses. In this study, a simulated numerical analysis was performed in which the catalyst bed was modeled as a one-dimensional porous medium. The resulting physical phenomena were examined by considering variations in catalyst bed characteristics incurred by catalyst pellet failure. From observations of various hot-firing experiments, it was determined that the upper region of the decomposition chamber was preferentially damaged in failure situations, which led to the conclusion that catalyst failure occurs in the upper region only. We simulated various cases based on the crushing and mass loss of catalyst pellets. The distributions of temperature, species mass fraction, heterogeneous reaction rate, and pressure were calculated after catalyst bed failure. The pressures at the decomposition chamber exit and the thrust at the nozzle exit were monitored with time. Through these analyses, the thermochemical phenomena inside a hydrazine monopropellant thruster system were interpreted in detail.

1. INTRODUCTION

Thruster systems are used for orbit correction and attitude control of satellites and spacecraft. Thrust can be produced with several different propulsion methods, including cold gas, monopropellant, bipropellant, electrical, and solid propulsion. Among these, monopropellant thrusters are often employed for satellite maneuverability, because of their high reliability. In the early days of spacecraft, hydrogen peroxide was used as a monopropellant, but hydrogen peroxide tends to self-decompose, even under the best storage conditions,¹ so alternatives were sought thereafter. Today, hydrazine monopropellant thrusters have largely replaced hydrogen peroxide monopropellant thrusters. Hydrazine can be controllably decomposed using catalyst metals such as iridium and platinum, and the spontaneous ignition characteristics of hydrazine in the presence of these metals have led to thruster systems that are both simpler and more reliable than conventional bipropellant thruster systems. In particular, hydrazine monopropellant thruster systems have been widely used for space applications that require very high reliability; various sizes of hydrazine monopropellant thrusters have been used on satellites and spacecraft launcher vehicles over the past few decades to control and correct altitude.^{1,2}

Iridium catalysts have been widely used in hydrazine monopropellant thrusters since the successful development in the 1960s of the Shell 405 catalyst by the Shell Oil Company.

Other hydrazine decomposition catalysts include CNESRO and KC 12 GA, developed by France and Germany, respectively. Today, the Shell 405 catalyst is manufactured by Aerojet and marketed under the name S-405 catalyst, and the KC 12 GA catalyst has been reproduced H-KC 12 GA by the German company W.C. Heraeus of Hanau.^{1,3} The catalyst is the most important element of a monopropellant thruster system, because it controls propellant decomposition, which determines the overall thruster performance. Various test processes are conducted to evaluate decomposition performance in a catalyst bed.^{4,5} For example, the catalyst pellets are thermally stressed repeatedly by both pulse mode operation and cold starts. These stresses can cause fracture of the catalyst pellets, reducing their total mass in the bed as some fractured catalyst pieces are washed away. For this reason, the mass loss rate of a catalyst is usually specified as an important performance variable of different grades of catalyst pellets.^{3–5}

The testing and handling procedures for hydrazine monopropellant thrusters are usually complicated because of the toxicity of hydrazine and its decomposition product gases.⁶

Received: October 13, 2011

Revised: March 26, 2012

Accepted: March 26, 2012

Published: April 6, 2012

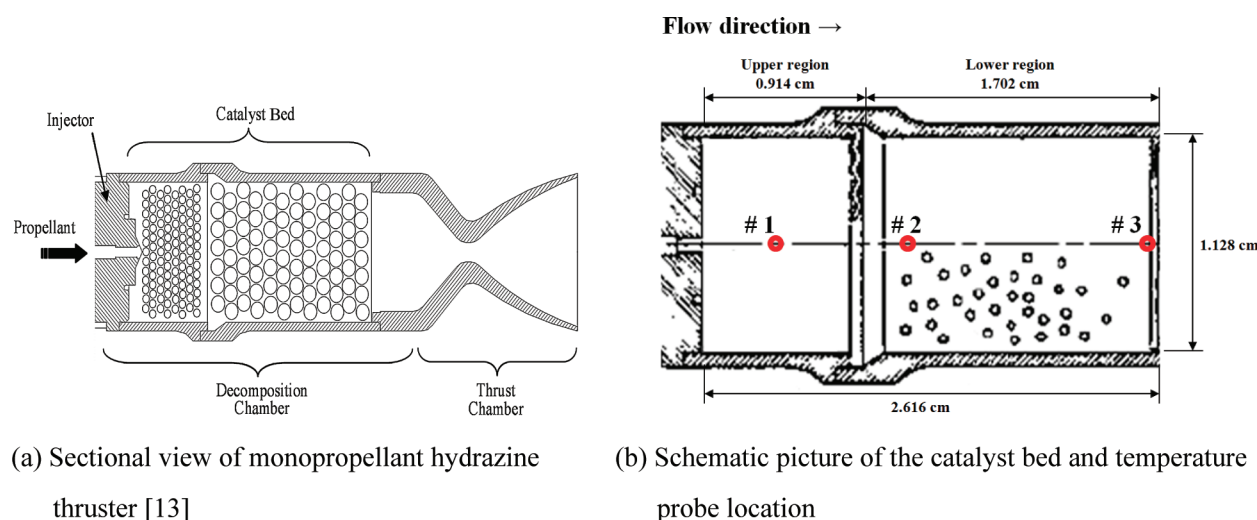


Figure 1. Schematic picture of a satellite thruster. (From ref 13; used with permission.)

Thus, numerical analysis that improves the understanding of the effects of various thruster design parameters can reduce engineering and design times as well as expenses. It is difficult to collect detailed data during actual thruster operation, so well-validated simulation codes are required to determine what happens inside a thruster system. Kesten⁷ studied a numerical simulation model during development of the Shell 405 catalyst. He suggested that the gas-phase and solid-phase governing equations indicated that the reaction chamber could be viewed as one-dimensional porous medium. Crespo⁸ calculated the specific impulse of a hydrazine thruster based on ammonia decomposition and proposed a correlation equation for the hydrazine and ammonia decomposition ratios. He also proposed correlation equations for species mass fraction at the end of the vaporization region. Shankar et al.⁹ derived a set of gas and liquid-phase steady-state governing equations for the induction region of the injected hydrazine. They referred the correlation equations, which were proposed by Crespo,⁸ to predict the species mass fraction at the vaporization region. As a consequence, they simulated various cases according to thruster size, bed loading, and chamber inlet pressure, and also utilized the results of their numerical analyses to design a 10 N thruster.¹⁰ Makled and Belal¹¹ compared the ammonia dissociation fraction and gas temperature inside the catalyst bed using the correlation equation of Kesten¹² and a two-step chemical reaction calculation. Han et al.¹³ conducted a hot-firing test using a hydrazine thruster developed by the Korea Aerospace Research Institute (KARI) and tabulated the measured chamber temperature, pressure, and propellant mass flow rate. They developed polynomial equations for the propellant mass flow rate, chamber pressure, and chamber temperature as functions of the inlet pressure. They then used these values to set the inlet boundary conditions for a two-dimensional nozzle analysis.

The purpose of this study is to simulate catalyst pellet failure and to determine the differences in thermochemical phenomena between normal operation and catalyst bed failure operation. To achieve this objective, the catalyst bed was modeled as a one-dimensional porous medium. The resulting physical phenomena were then used to determine

how variations in the catalyst bed characteristics relate to catalyst pellet failure.

2. PHYSICAL PHENOMENA CHANGES ACCORDING TO CATALYST BED FAILURE

A ground test was conducted using a KARI hydrazine thruster based on an iridium-coated alumina catalyst pellet. The total length of decomposition chamber of the thruster was 2.616 cm, which was divided into two parts: an upper region (near the injector) and a lower region. Different sizes of catalyst were placed in each region, and a screen separated the regions. Detailed information for the KARI hydrazine thruster used in this study can be found in Han et al.,¹³ and a schematic diagram of the thruster is shown in Figure 1. The catalyst charged in the decomposition chamber is a new iridium catalyst pellet KCMC-7,¹⁴ which was manufactured in Clean Energy Technology Laboratory at the Chonnam National University (located in the city of Gwangju, ROK) and KARI. The feature of catalyst pellet can be described with four parameters: pore volume = 0.18 cm³/g, BET specific surface area = 125 m²/g, average pore size = 16.7 nm, and iridium loading = 33.0 wt %. The detailed fabrication procedures are described well in the work of Jang et al.¹⁴ In numerous experiments, we observed that repetitive thermal stresses caused catalyst pellets in the upper region to crack. Small, broken catalyst particles were washed away, leaving empty space upstream of the catalyst bed, as shown in Figure 2. Therefore, the total mass of catalyst was reduced, and a maximum mass loss rate of 15.05% was reported.¹⁵ Catalyst bed failure was not observed in the lower region of the decomposition chamber, because there was less thermal stress therein than in the upper region.

We observed large fluctuations in chamber exit pressure upon bed failure (see Figure 3a, which compares normal operation to the failure case). Catalyst mass loss and pressure variations could be correlated to two catalyst bed characteristics:

- Changes in size of the catalyst pellets due to cracking
- Changes in the porosity of the catalyst bed

In several experiments, the combination of these two characteristics caused catalyst bed failure. In the first case, pellets in the upper region cracked, remained in the upper region, and were not washed away from the catalyst bed. In this

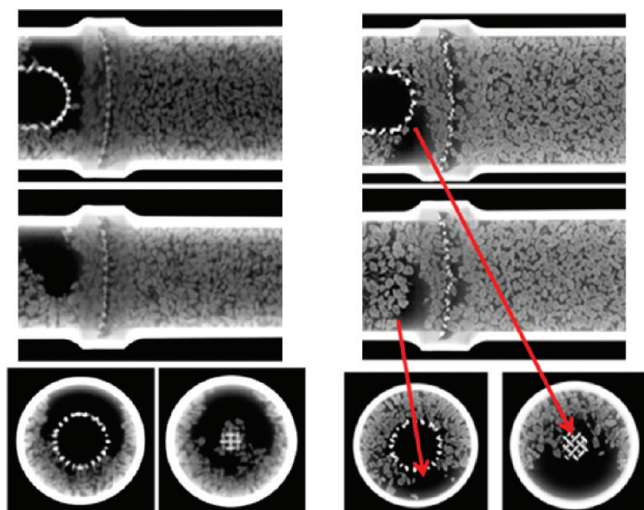


Figure 2. Pictures of catalyst bed failure.

situation, the size of catalyst pellets in upper region was reduced, but the porosity of the catalyst bed was not changed. If, however, the pellets were cracked further, some smaller pellet pieces escaped the catalyst bed. In this case, both the pellet size and the catalyst bed porosity in the upper region were changed simultaneously. The properties of the lower region were not changed in either of these situations. However, if instead some small pellet particles remained in the interstitial spaces between the lower region pellets, the porosity of the lower catalyst bed could also be reduced. The total mass of the catalyst pellets was calculated using eq 1:¹⁶

$$W_{\text{catalyst}} = \rho_{\text{catalyst}}(1 - \varepsilon)V_{\text{chamber}} \quad (1)$$

Because the density of the catalyst and the chamber volume does not change, any loss of catalyst mass is controlled by varying the porosity of the catalyst bed.

3. COMPUTATIONAL METHOD

In this study, we separated a satellite thruster into two parts: the catalyst bed and the nozzle section. Because the decomposition chamber was filled with catalyst pellets, the catalyst bed was modeled as a one-dimensional porous medium.⁷

3.1. Catalyst Bed Region Model. The governing equations for the catalyst bed were separated into catalyst-surface equations (eqs 2–6) and gas-phase equations (eqs 7–11).^{7,9}

One of the most important properties for characterizing transport phenomena between catalyst pellets and the gas phase is the specific surface area. In our study, the specific surface area was defined as the ratio of the pellet surface area to the pellet volume, and it could be varied with respect to catalyst bed porosity and pellet size. The sphericity of the catalyst pellet ϕ_s was assumed to be 0.75.⁹

Catalyst-surface equations:

$$\frac{dT_s}{dt} = -\frac{1}{\rho_s C_s} \left[(Hr_{het})^{N_2H_4} + (Hr_{het})^{NH_3} \right] + \frac{3h_c}{d_p \rho_s C_s} (T_g - T_s) \quad (2)$$

$$\frac{dY_s^{N_2H_4}}{dt} = -\frac{1}{\varepsilon_p} r_{het}^{N_2H_4} + \frac{3k_c^{N_2H_4}}{\varepsilon_p d_p} (Y_g^{N_2H_4} - Y_s^{N_2H_4}) \quad (3)$$

$$\frac{dY_s^{H_2}}{dt} = \frac{1}{\varepsilon_p} \left[r_{het}^{N_2H_4} \frac{M^{H_2}}{2M^{N_2H_4}} + r_{het}^{NH_3} \frac{3M^{H_2}}{2M^{NH_3}} \right] + \frac{3k_c^{H_2}}{\varepsilon_p d_p} (Y_g^{H_2} - Y_s^{H_2}) \quad (4)$$

$$\frac{dY_s^{NH_3}}{dt} = \frac{1}{\varepsilon_p} \left[r_{het}^{N_2H_4} \frac{M^{NH_3}}{2M^{N_2H_4}} - r_{het}^{NH_3} \right] + \frac{3k_c^{NH_3}}{\varepsilon_p d_p} (Y_g^{NH_3} - Y_s^{NH_3}) \quad (5)$$

$$\frac{dY_s^{N_2}}{dt} = \frac{1}{\varepsilon_p} \left[r_{het}^{N_2H_4} \frac{M^{N_2}}{2M^{NH_3}} + r_{het}^{NH_3} \frac{M^{N_2}}{2M^{NH_3}} \right] + \frac{3k_c^{N_2}}{\varepsilon_p d_p} (Y_g^{N_2} - Y_s^{N_2}) \quad (6)$$

Gas-phase equations:

$$GC_{p,g} \frac{dT_g}{dZ} = -A_p h_c (T_g - T_s) - \frac{4h_c}{d_c} (T_g - T_w) \quad (7)$$

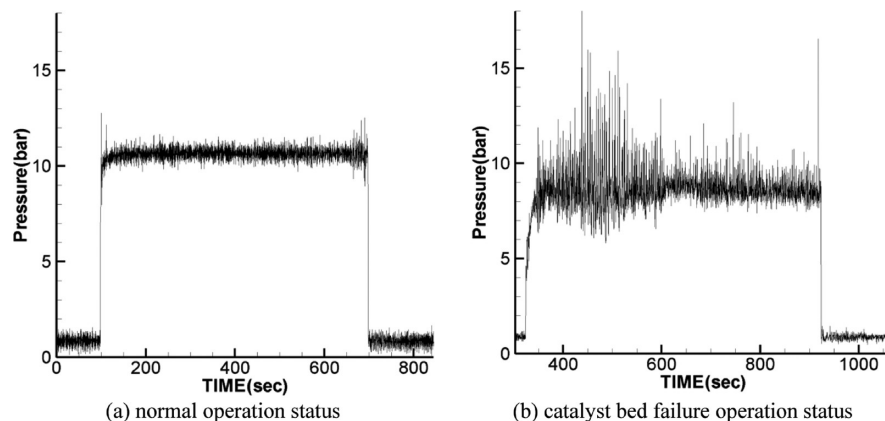


Figure 3. Comparison of experimental pressure data.

$$\frac{G}{\rho^i} \frac{dY_g^i}{dZ} = -A_p k_c^i (Y_g^i - Y_s^i) \quad (8)$$

$$h_c = 0.74 \left[\frac{A_p \mu}{G} \right]^{0.41} C_p G \quad (9)$$

$$k_c^i = \left[\frac{A_p \mu}{G} \right]^{0.41} \left[\frac{0.61 G}{\rho^i} \right] \left[\frac{\rho^i D^i}{\mu^i} \right]^{0.667} \quad (10)$$

$$G \equiv \frac{\text{mass flow rate of mixture}}{\text{cross-sectional area of chamber}} \quad (11)$$

where

$$A_p = \frac{6(1 - \varepsilon)}{\phi_s d_p} \quad i = \text{N}_2\text{H}_4, \text{H}_2, \text{NH}_3, \text{N}_2 \quad (11)$$

Because some length is required for vaporization of injected liquid hydrazine, an induction region was included in the thruster design. Shankar et al.⁹ defined the induction region for vaporization and derived an energy equation to govern it. At the end of the induction region, the mass fraction of hydrazine was predicted and the mass fractions of the other species were determined based on hydrazine decomposition stoichiometry (eqs 12 – 17).

$$\frac{dT_g}{dZ} = \left(\frac{\Delta H_r \text{N}_2\text{H}_4 - L \text{N}_2\text{H}_4}{GC_p} \right) A_p P_{vr} \text{N}_2\text{H}_4 \left(\frac{M \text{N}_2\text{H}_4}{R_u T} \right) \times \sqrt{D \text{N}_2\text{H}_4 A} \exp \left[\frac{\left(-L \text{N}_2\text{H}_4 / R_u \right) + (T_A / 2)}{T} \right] \quad (12)$$

$$Z_{\text{induction}} = \left(\frac{1}{C} \right) \frac{T_0^2}{(L/R_u) + (T_A/2)} \quad \text{where } C = \text{RHS of eq 12 for } T = T_0 \quad (13)$$

$$Y_g^{\text{N}_2\text{H}_4} = 0.87 - 0.0006 T_{\text{induction}} \quad (14)$$

$$Y_g^{\text{NH}_3} = \left(\frac{M^{\text{NH}_3}}{M^{\text{N}_2\text{H}_4}} \right) (1 - Y_g^{\text{N}_2\text{H}_4}) \quad (15)$$

$$Y_g^{\text{N}_2} = \left(\frac{M^{\text{N}_2}}{2M^{\text{N}_2\text{H}_4}} \right) (1 - Y_g^{\text{N}_2\text{H}_4}) \quad (16)$$

$$Y_g^{\text{H}_2} = \left(\frac{M^{\text{H}_2}}{2M^{\text{N}_2\text{H}_4}} \right) (1 - Y_g^{\text{N}_2\text{H}_4}) \quad (17)$$

The pressure drop through the catalyst bed was calculated using the modified Ergun equation (eqs 18 and 19), which were proposed by Macdonald et al.¹⁷

$$\frac{dP}{dZ} = \mu \left[\frac{180(1 - \varepsilon)^2}{\varepsilon^3 d_p^2} \right] V_{\text{darcy}} + \rho \left[\frac{4(1 - \varepsilon)}{\varepsilon^3 d_p} \right] V_{\text{darcy}}^2 \quad (18)$$

where

$$V_{\text{darcy}} = \frac{G}{\rho} \quad (19)$$

3.2. Nozzle Region Model. Equations 20–27 are gas-phase equations for two-dimensional axisymmetric gas flow.^{18,19}

$$\Gamma \frac{\partial Q}{\partial t} + \frac{\partial(E - E_V)}{\partial Z} + \frac{\partial(F - F_V)}{\partial R} = \alpha H \quad (20)$$

In eq 20, Γ represents the preconditioning matrix and controls the eigenvalues; E and F are flux terms, and E_V and F_V are diffusive terms. H is an axisymmetric term; α has a value of 0 for a two-dimensional problem and 1 for an axisymmetric problem. Because subsonic and supersonic flows exist in the nozzle, the preconditioning method was applied. The preconditioning method is known to have good convergence characteristics throughout the entire flow speed regime.¹⁸

$$\Gamma = \begin{Bmatrix} \rho_p & 0 & 0 & \rho_T & 0 & 0 & 0 \\ \rho_p u & \rho & 0 & \rho_T u & 0 & 0 & 0 \\ \rho_p v & 0 & \rho & \rho_T v & 0 & 0 & 0 \\ \rho_p H - 1 & \rho u & \rho v & \rho_T H + \rho C_p & 0 & 0 & 0 \\ \rho_p \kappa & 0 & 0 & \rho_T \kappa & \rho & 0 & 0 \\ \rho_p \omega & 0 & 0 & \rho_T \omega & 0 & \rho & 0 \\ \rho_p Y_i & 0 & 0 & \rho_T Y_i & 0 & 0 & \rho \end{Bmatrix} \quad (21)$$

$$Q = \{p, u, v, T, \kappa, \omega, Y_i\}^T \quad (22)$$

$$E = \{\rho u, \rho u^2 + p, \rho uv, \rho uH, \rho u\kappa, \rho u\omega, \rho uY_i\}^T \quad (23)$$

$$E_V = \{0, \tau_{zz}, \tau_{zr}, u\tau_{zz} + v\tau_{zr} + q_z, \tau_{\kappa z}, \tau_{\omega z}, \rho \hat{u}Y_i\}^T \quad (24)$$

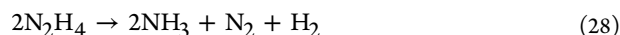
$$F = \{\rho v, \rho uv, \rho v^2 + p, \rho vH, \rho v\kappa, \rho v\omega, \rho vY_i\}^T \quad (25)$$

$$F_V = \{0, \tau_{zr}, \tau_{rr}, u\tau_{zr} + v\tau_{rr} + q_r, \rho \hat{v}\kappa, \rho \hat{v}\omega, \rho \hat{v}Y_i\}^T \quad (26)$$

$$H = \frac{1}{2}(u^2 + v^2) + \sum_{i=1}^N Y_i h_i \quad (27)$$

To solve the axisymmetric nozzle flow, a modified advective upwind splitting method (AUSM⁺-up)²⁰ was used to address the flux term in the Navier–Stokes equations. The shear-stress transport turbulent model was used to close the Navier–Stokes equations.²¹ The boundary conditions at the nozzle inlet were determined at the catalyst chamber exit, and a no-slip condition was used at the wall and a symmetric condition was used at the axisymmetric axis. Calculated values at the chamber exit were extrapolated using information from the previous grid, because the flow speed at the divergence section of the nozzle was supersonic.

3.3. Chemical Kinetics Model. The decomposition kinetics of hydrazine can be described by a two-step reaction model (eqs 28 and 29):



Numerous researchers have proposed an Arrhenius-type reaction constant, i.e., a pre-exponential factor A and an activation energy E_a or activation temperature T_a for a heterogeneous reaction of hydrazine and ammonia.^{7–9,11,12,22} It is important to use the proper reaction constants when carrying out numerical analysis. The kinetic parameters used by Kesten,⁷ as well as Shankar et al.,⁹ were also empirically determined by trial and error. The new catalyst pellet developed by Jang et al.¹⁴ was charged into the KARI thruster. Therefore, the activation energy value 2777.78 K, which fall into the range over 2939 ± 1079 K decided empirically by experiment,²² is used as a reference.¹¹ The activation energy and activation temperature of hydrazine decomposition are much lower than those of ammonia decomposition, which indicates that hydrazine decomposition is more active. Hence, hydrazine decomposition kinetics control the entire catalytic combustion process inside the thruster. The pre-exponential factor A , which varies depending upon the system configuration, includes a steric factor that can be illustrated by considering the collision of the reacting molecules.²³ The reaction rate terms of eqs 2–6 can be expressed as shown in eqs 30 and 31.

$$r_{\text{het}}^{\text{N}_2\text{H}_4} = 1.5 \times 10^4 \exp\left(-\frac{2777.78}{T_s}\right) Y^{\text{N}_2\text{H}_4} \quad (30)$$

$$r_{\text{het}}^{\text{NH}_3} = 2.53 \times 10^{10} \exp\left(-\frac{2777.78}{T_s}\right) Y^{\text{NH}_3} \quad (31)$$

3.4. Thermodynamic and Transport Properties. Both the specific heat ratio and the enthalpy are functions of temperature and can be calculated using the polynomial coefficients proposed by Zehe et al.²⁴ (eqs 32 and 33):

$$\frac{C_{p,i}(T)}{R_u} = a_{1,i}T^{-2} + a_{2,i}T^{-1} + a_{3,i} + a_{4,i}T^1 + a_{5,i}T^2 + a_{6,i}T^3 + a_{7,i}T^4 \quad (32)$$

$$h_i = h_{f,i}^0 + \int_{T_{\text{ref}}}^T C_{p,i}dT \quad (33)$$

The properties of liquid hydrazine were taken from Daubert's and Danner's data compilation book.²⁵ The properties of the gas-phase species (i.e., hydrazine, ammonia, hydrogen, and nitrogen) were calculated using the method developed by Kee et al.²⁶

4. RESULTS AND DISCUSSION

4.1. Code Validation. To validate the code for catalyst bed and nozzle analysis developed herein, calculated results were compared with experimental data. The temperature measurement locations in the decomposition chamber are shown in Figure 1b, and the result of each probe location is displayed in Figure 4. The inlet conditions of the thruster used to perform the experiment were as follows: inlet pressure, 26.7 bar; mass flow rate, 2.06 g/s; and inlet temperature, 300 K.

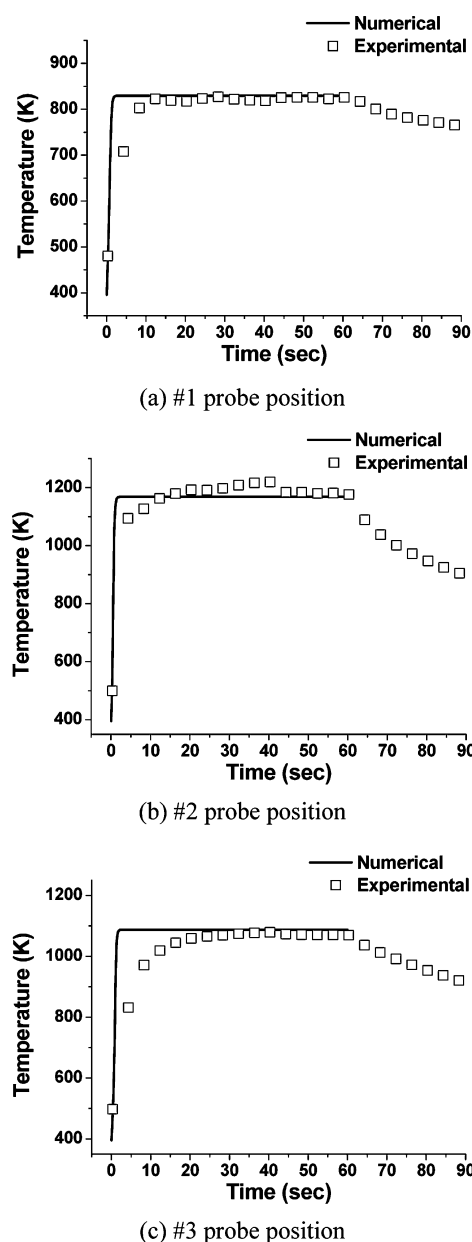


Figure 4. Validation of the catalyst bed code.

Although there was good agreement for steady-state conditions, there were some discrepancies between the experimental and calculated data for the transient state. Discrepancies were attributed to factors such as the response time of the thermocouple, heat loss through the chamber casing, probe position, and numerical errors made during the transient period. By comparing the experimental and calculated data, we concluded that the developed code could adequately reproduce the catalytic combustion phenomena in the catalyst bed.

The nozzle code was validated according to nozzle flow methods developed by the Jet Propulsion Laboratory (JPL) at the California Institute of Technology. Figure 5 shows the computational grid used and the resulting Mach number contours. The calculated pressure variation values were compared with the experimental data from Cuffel et al.²⁷ As shown in Figure 6, the data were in good agreement.

4.2. Effects of Catalyst Bed Failure. Cases 1 and 2 were used to verify the effects of failure caused by catalyst pellet

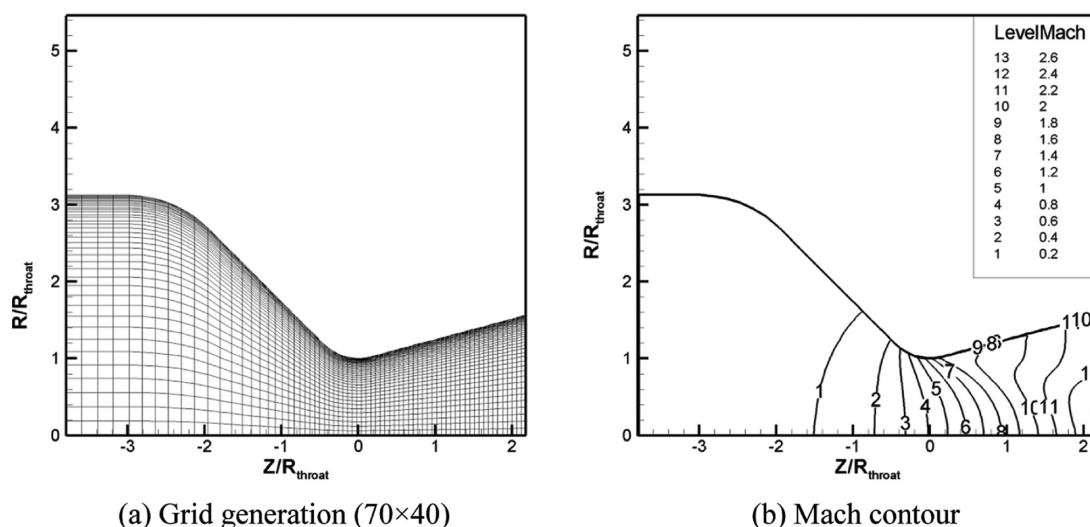


Figure 5. Grid and mach contour for the JPL nozzle.

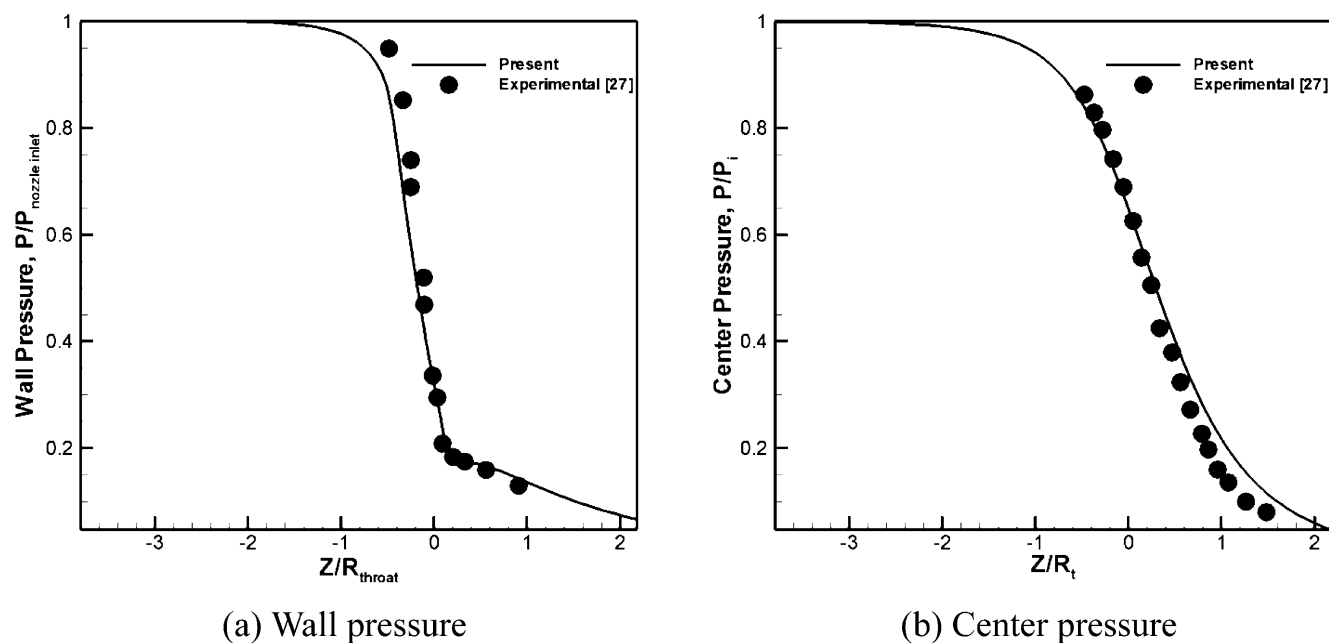


Figure 6. Comparison of pressure variation.

size reduction. Case 1 was for normal operation, and cases 2-1, 2-2, and 2-3 were simulated failures, in which the sizes of the pellets in the upper region were reduced from the beginning of the catalyst bed. The catalyst bed failure ratio can be defined as a ratio of the failed length from 0 cm to the total catalyst bed length. The catalyst bed failure ratio of cases 2-1, 2-2, and 2-3 were set to 10%, 20%, and 30%, respectively. The total operation time was set to 60 s, and the catalyst bed properties of cases 2-1, 2-2, and 2-3 were equal to that of case 1 for the first 30 s. After 30 s, the properties were changed. However, mass loss was not considered in these cases.

Case 3 simulated the failure situation in which the loss of catalyst pellets took place in the entire upper region. The length of upper region accounts for 35% of the total catalyst bed length. Therefore, the catalyst bed failure ratio for case 3 was set to 35% with a simultaneous change in the porosity. Case 3-1 examined the effects of catalyst mass loss in the

upper region with no mass increase in the lower region of the catalyst bed. In cases 3-2 and 3-3, some mass increase in the lower region was considered, caused by small particles that were washed from the upper region into the lower region of the catalyst bed. Most of the mass loss occurred in the upper region, and the mass loss rate was limited to 15%, which is the maximum value reported by Kim et al.¹⁵ The pellet size did not change in case 3, so only the effects of catalyst mass loss were examined. Detailed conditions for these simulations are summarized in Table 1.

4.2.1. Catalyst Bed Failure without Mass Loss (Cases 2-1, 2-2, and 2-3). Figure 7 represents the steady-state temperature distribution and the heterogeneous reaction rate after catalyst bed failure. The peak temperature location inside the catalyst bed moved to the upstream region as the severity of the failure increased. Because the catalyst pellets were composed of fine alumina powder, and because the iridium-loading rate reached 33%, crushing of the pellets incre-

Table 1. Changes in Catalyst Bed Properties after 30 s

case	catalyst bed failure ratio (%)	Failure Bed		Remaining Bed		catalyst mass loss rate (%)
		pellet diameter (mm)	porosity	pellet diameter (mm)	porosity	
1	0	1	0.4	1	0.4	0
2-1	10	0.6	0.4	1	0.4	0
2-2	20	0.6	0.4	1	0.4	0
2-3	30	0.6	0.4	1	0.4	0
3-1	35	1	0.658	1	0.4	15
3-2	35	1	0.658	1	0.354	10
3-3	35	1	0.844	1	0.3	15

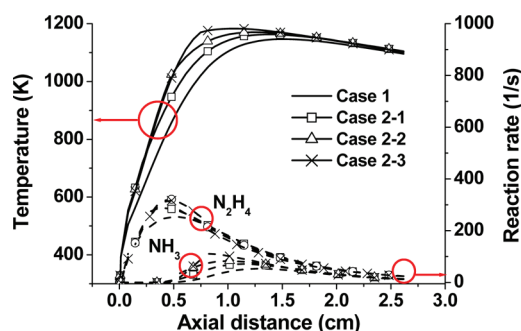


Figure 7. Comparison of temperature (solid line) and heterogeneous reaction rate (dashed line) after catalyst bed failure without mass loss.

mentally increased the contact surface area between the hydrazine (or ammonia) and the Ir catalyst, i.e., the specific surface area (A_p) increased, which is consistent with expectations based on eq 11. The reaction rate of hydrazine in the presence of crushed pellets was higher than during normal operation. Thus, in Figure 8,

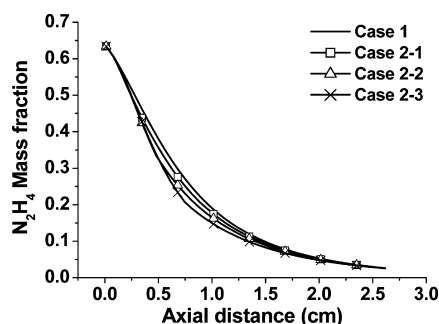


Figure 8. Comparison of hydrazine mass fraction after failure without mass loss.

more hydrazine decomposition at the same axial distance released more heat, leading to higher temperature values. The maximum calculated temperature deviation was 174.6 K at 0.55 cm. However, the temperature deviation at the end of the chamber was relatively small at only ~20 K. This phenomenon is explained by the differences in the reaction rate and the species mass fraction distribution of ammonia, as shown in Figures 7 and 9.

The presence of smaller catalyst pellets accelerated not only hydrazine decomposition but also ammonia decomposition. Because ammonia decomposition is endothermic, the temperature decreased after the hydrazine decomposition reaction started to slow down. As shown in Figure 9, the ammonia mass fraction during catalyst bed failure was initially higher than during normal operation because faster

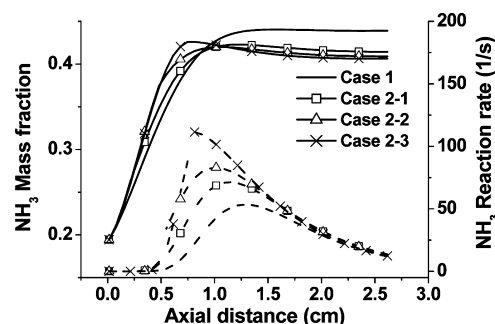


Figure 9. Comparison of ammonia mass fraction (solid line) and heterogeneous reaction rate (dashed line) after catalyst bed failure without mass loss.

decomposition of hydrazine generated more ammonia gas. Eventually, however, the decomposition of ammonia into hydrogen and nitrogen dominated, and the ammonia mass fraction decreased. For this reason, the ammonia mass fraction in Figure 9 was lower after 0.95 cm, when compared to normal operation.

The pressure drop in the decomposition chamber was also affected by catalyst bed failure. The pressure at the end of the catalyst bed and the thrust at the nozzle exit are shown in Figure 10. After 30 s, the pressure began to decrease as the

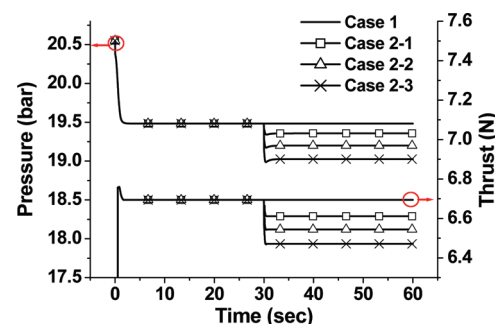


Figure 10. Comparison of pressure at the catalyst bed and thrust at the nozzle exit during operation time without mass loss.

catalyst damage became more severe. The temperature was only slightly higher, by not more than 20 K, at the end of the combustion chamber compared to normal operation. Because the temperatures were similar at the nozzle inlet for each simulated case, the calculated thrust followed the same trend with respect to pressure. The thrust calculated by the axisymmetric two-dimensional code did not vary greatly. In contrast, the axial velocity contours for each case, the axial and radial velocity distributions along the radial direction at the nozzle axis at time of 60 s, as shown in Figures 11 and 12, were quite different. The actual downstream environment of the nozzle exit is space, i.e., a vacuum, so that the continuum approach using the Navier–Stokes equations might not be adequate for predicting the plume. For more accurate prediction of the plume in a vacuum (or rarefied) environment, the Direct Simulation Monte Carlo (DSMC) method may be suggested for use instead. The results shown in Figures 11 and 12 can incur abnormal plume formation at the downstream of nozzle exit. Abnormal plume formation downstream of the nozzle exit can affect the thruster performance in a vacuum; possible adverse effects include disturbance forces or torques on the satellite attitude, thermal loads, and

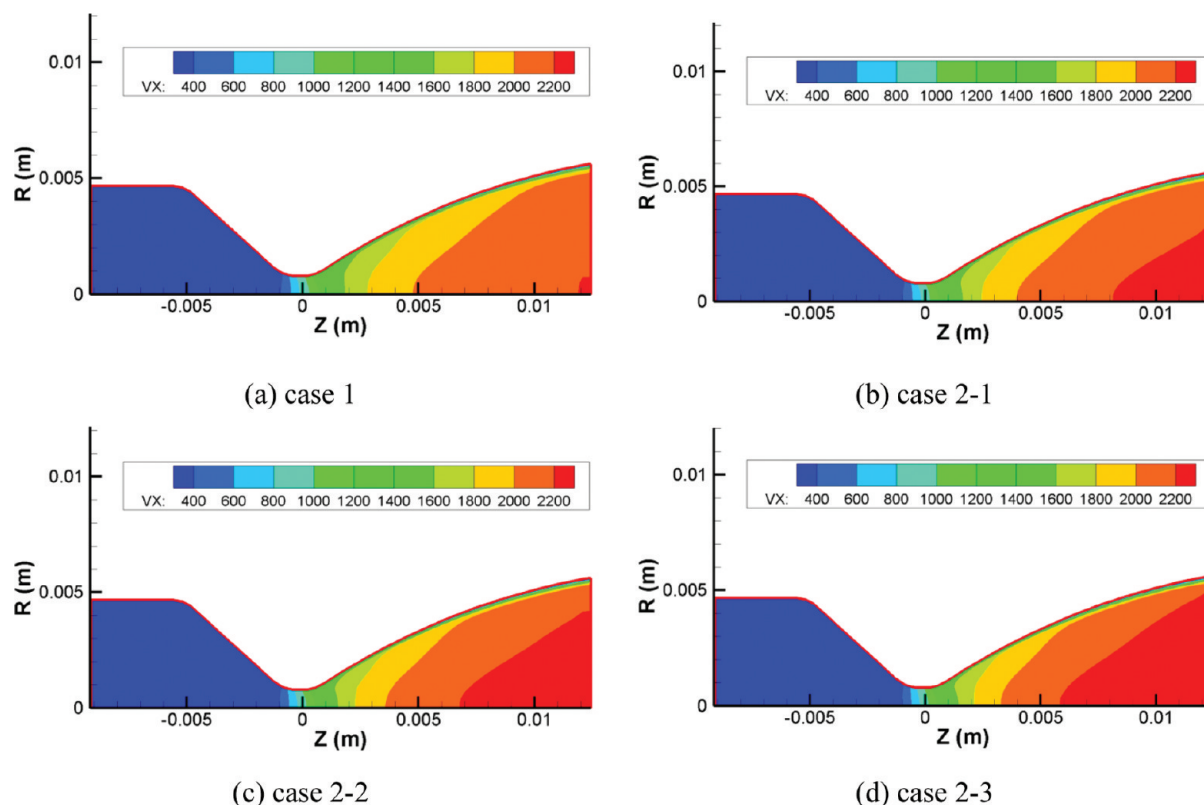


Figure 11. Comparison of axial velocity after catalyst bed failure without mass loss at time of 60 s (velocity unit: m/s).

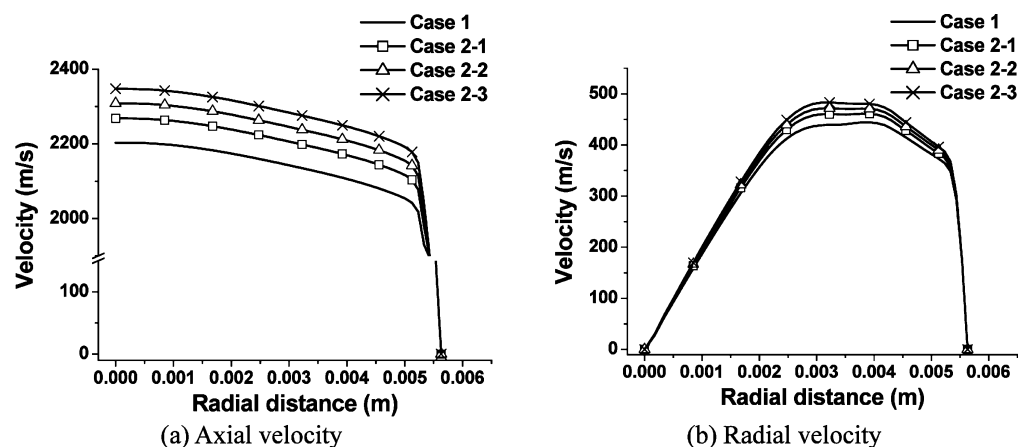


Figure 12. Comparison of velocity along the radial direction at the nozzle exit at time of 60 s.

contamination of sensitive surfaces.²⁸ Therefore, accurate plume prediction is critical to the design of an effective satellite thruster system. The overall thruster design is outside the scope of this paper, but the nozzle exit results obtained herein could be utilized to determine the inlet conditions for the DSMC method.

Predictions for the pressure drop inside the catalyst bed are shown in Figure 13. The total pressure drop through the catalyst bed was calculated to be about 1.3 bar. As noted in section 2, we considered the catalyst bed failure from the starting point of thruster. Therefore, the pressure gradient in the downstream failure region, indicated by the dashed line, was more severe than for a catalyst bed under normal conditions; after the failure region, the pressure drop behavior returned to that observed for a catalyst bed under normal operation.

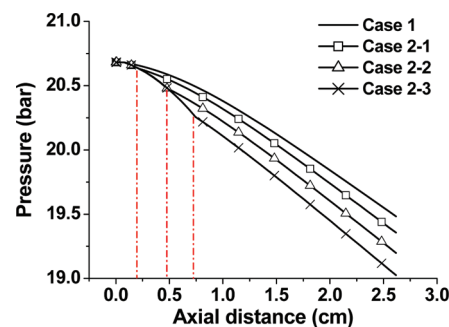


Figure 13. Comparison of pressure drop along the catalyst bed axis without mass loss at time of 60 s.

4.2.2. Catalyst Bed Failure with Mass Loss (Cases 3-1, 3-2, and 3-3). When catalyst pellet loss occurred in the upper

region, the observed behavior was different from that of the cases discussed previously in section 4.2.1. In particular, the increase in temperature was delayed. When catalyst pellet loss occurred in the upper region, the hydrazine did not decompose as fast, and the heat released by hydrazine decomposition was lower than that observed during normal operation. However, after propellant passed through the destroyed upper region, hydrazine decomposition occurred more rapidly in the lower region of the chamber. The heterogeneous reaction rate shown in Figure 14 and the remaining hydrazine

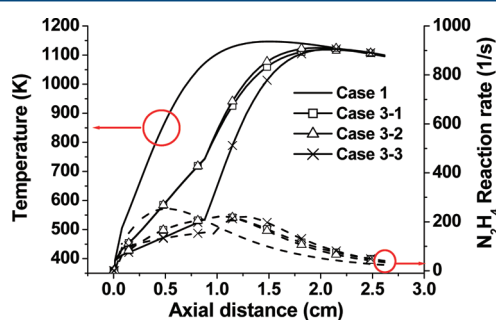


Figure 14. Comparison of temperature (solid line) and heterogeneous reaction rate (dashed line) after catalyst bed failure with mass loss.

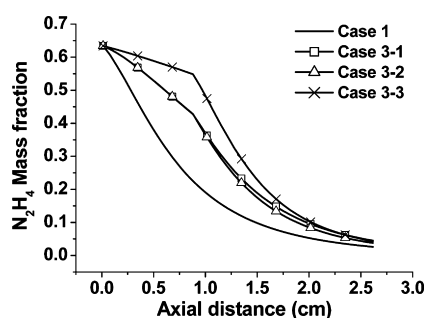


Figure 15. Comparison of hydrazine mass fraction after catalyst bed failure with mass loss.

mass fraction shown in Figure 15 supported our interpretation. While hydrazine decomposition and temperature rise were suppressed, the chamber exit temperature exhibited almost the same value, because the mass loss of catalyst in the upper region suppressed not only the decomposition of hydrazine (an exothermic reaction) but also the decomposition of ammonia (an endothermic reaction). As shown in Figure 16, the

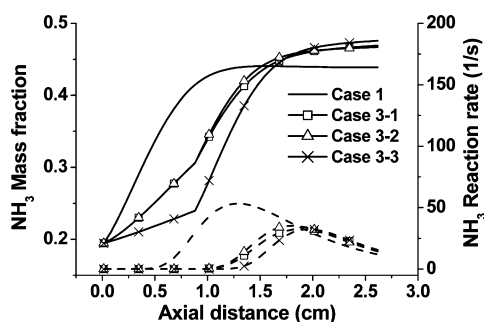


Figure 16. Comparison of ammonia mass fraction (solid line) and heterogeneous reaction rate (dashed line) after catalyst bed failure with mass loss.

ammonia decomposition rate distributions of case 3 were retarded downstream and had lower values, compared to normal operation. Therefore, the ammonia mass fractions at the bed exit of case 3 were higher. However, the injected hydrazine was almost completely decomposed in the decomposition chamber, regardless of the failure of the catalyst bed. As a result, temperature changes in the lower region were reduced through a combination of these opposing phenomena.

The variations in pressure behaviors were quite different from previous cases. In case 3-1, the chamber exit pressure was larger than that in case 1 (normal operation), as shown in Figure 17. As shown in Figure 18, the loss of catalyst pellets in

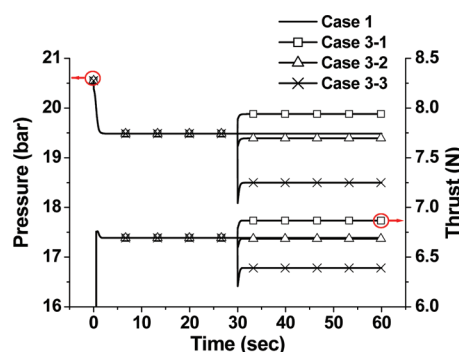


Figure 17. Comparison of pressure at the catalyst bed and thrust at the nozzle exit during operation.

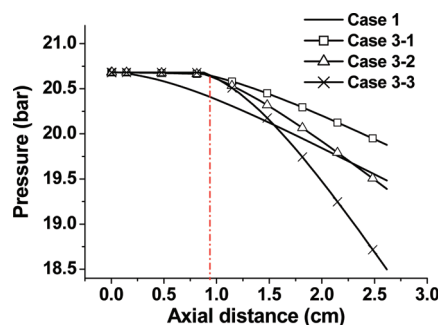


Figure 18. Comparison of pressure drop along the catalyst bed axis with mass loss at time of 60 s.

the upper region led to a reduction in pressure, compared to normal operation, because the fluid inside the upper region experienced reduced resistance. All of the subcases of case 3 (cases 3-1, 3-2, and 3-3) had higher porosity than case 1, so the pressure drop in the upper region was relatively small. However, after passing through the upper region, the pressure distribution of each case differed according to the porosity of the lower region.

Case 3-1 assumed that small pieces of cracked catalyst pellets from the upper region were washed away from the catalyst bed during operation. The loss rate was set to 15% of the total catalyst weight. In this case, the porosity of the lower region did not change because the mass of catalyst pellets in the lower region did not increase. In contrast, in case 3-2, a portion of the cracked catalyst pellets were not washed away, but rather were caught in the space between particles in the lower region. In this case, the pellet loss rate was set to 10% of the total catalyst weight, and the porosity of the lower region decreased slightly. Therefore, the flow resistance was augmented, and there was a larger pressure drop than observed in case 3-1. Case 3-3 simulated

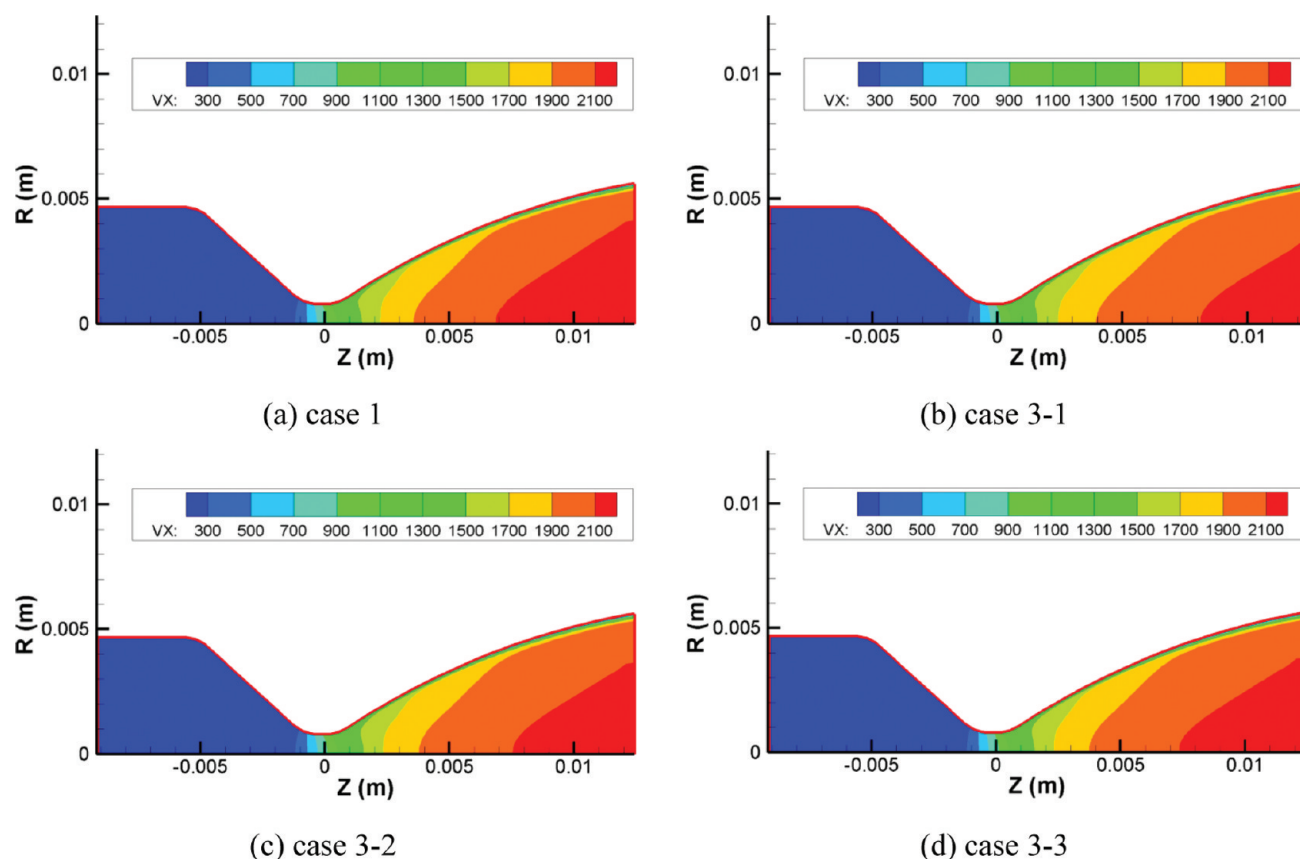


Figure 19. Comparison of axial velocity after catalyst bed failure without mass loss at time of 60 s (velocity unit: m/s).

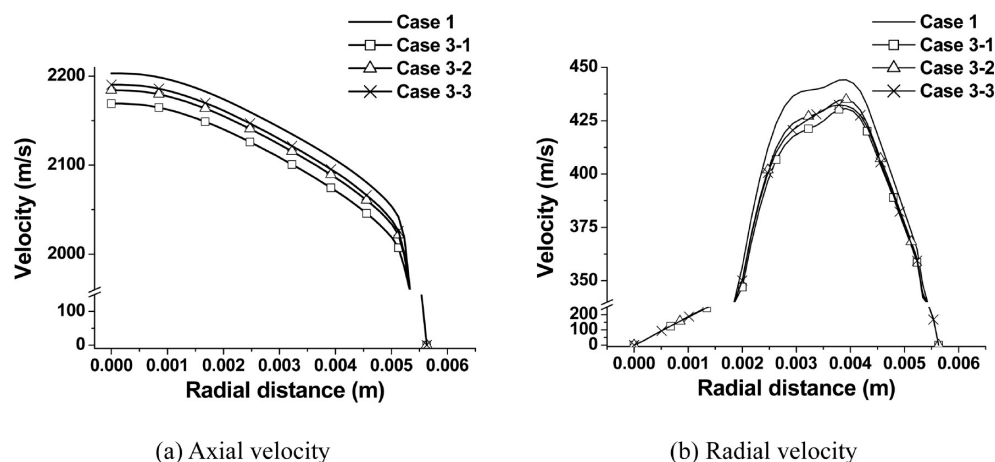


Figure 20. Comparison of velocity along the radial direction at the nozzle exit at time of 60 s.

increased cracking of catalyst pellets in the upper region and increased retention of cracked catalyst pieces in the lower region, compared to case 3-2. Consequently, while the pressure drop in the upper region was similar to that observed in cases 3-1 and 3-2, the pressure dropped more rapidly in the lower region, because of blockage. These pressure-drop tendencies affected the thrust variation at the nozzle exit. There were slight temperature differences at the chamber exit; as a consequence, the thrust changes varied in concert with the pressure variations. The predicted thrust values in case 3 were not significantly different from those predicted by case 2. Figures 19 and 20 depict the changes in the velocity distribution at the nozzle. As noted in section 4.2.1, these dis-

tribution changes can affect the plume behavior, and it is possible that abnormal disturbances can occur.

5. CONCLUSIONS

In this study, the thermochemical phenomena changes caused by catalyst bed failure were investigated by numerical simulation made possible by an analysis code. The thruster was separated into two components: the decomposition chamber and the nozzle section. Because of the differences between the fluid flow through porous media and nozzle flow, each section was modeled separately: the catalyst bed was modeled one-dimensionally and the nozzle was modeled

axisymmetrically and two-dimensionally. The developed codes were validated with experimental data. The catalyst bed was modeled by changing the pellet diameter and bed porosity. Catalyst bed failure could be classified in two ways, depending on the nature of the mass loss from loss of catalyst pellets. Through observation of numerous experiments in which catalyst bed failure occurred, it was determined that breakage of catalyst pellets occurred preferentially in the upper region of the decomposition chamber. Simulated experiments with validated codes were conducted based on this observation. As a consequence, the current study provides a better understanding of the thermochemical phenomena inside a hydrazine monopropellant thruster system. Our major results can be summarized as follows.

- (1) Catalyst bed failure occurred with concurrent changes in catalyst mass, which could be correlated to changes in catalyst size and catalyst bed porosity. The specific surface area (A_p), which corresponds to the interface between solid and gas phases where transport phenomena occur, was varied. The tendency for temperature to increase was dependent on the catalyst failure conditions; it either shifted rapidly upstream or was retarded downstream. Regardless of the temperature characteristics within the decomposition chamber, the temperatures at the chamber exit did not differ significantly in KARI thruster configurations. Because of the opposing combination of exothermic hydrazine decomposition and endothermic ammonia decomposition, the net heat release was balanced.
- (2) The hydrazine and ammonia mass fractions were also affected by the condition of the catalyst bed. Ammonia gas was generated from the decomposition of hydrazine, and it varied drastically, depending on the failure conditions.
- (3) The pressure drop in the decomposition chamber was affected by the Darcy velocity, which varied with density change, i.e., with different temperature distributions. However, the pressure drop was most influenced by the configuration characteristics of the catalyst bed (namely, pellet size and bed porosity). The thrust at the nozzle exit exhibited a similar pressure behavior because the temperature difference at the nozzle inlet did not differ significantly between simulated cases studied.
- (4) The velocity distribution affected the formation of a plume in a vacuum environment, which would result in abnormal disturbances in a satellite system. The results described in this paper can thus be utilized for design of inlet conditions for the Direct Simulation Monte Carlo (DSMC) method.

AUTHOR INFORMATION

Corresponding Author

*Tel.: +82-42-350-3714. Fax: +82-42-350-3710. E-mail: swbaek@kaist.ac.kr.

Notes

The authors declare no competing financial interest.

ACKNOWLEDGMENTS

This work was supported by grant of Strengthen Institute–Academia Collaboration of Korea Aerospace Research Institute.

NOMENCLATURE

Alphabets

A = pre-exponential factor [$1/s$]
 A_p = specific surface area [m^2/m^3]
 C_s = specific heat of catalyst [$J/kg \cdot K$]
 C_p = specific heat of gas [$J/(kg \cdot K)$]
 d_c = chamber diameter [m]
 d_p = particle diameter [m]
 D = diffusion coefficient [m^2/s]
 E = z flux vector
 E_V = z viscous vector
 F = r flux vector
 F_V = r viscous vector
 G = chamber bed loading [$kg/(m^2 \cdot s)$]
 h_c = heat-transfer coefficient [$J/(m^2 \cdot s \cdot K)$]
 h_i = enthalpy of species i [J/kg]
 ΔH_r = heat of reaction [J/kg]
 H = axisymmetric source term
 k_c = mass-transfer coefficient [m/s]
 L = latent heat [J/kg]
 M = molecular weight [kg/mol]
 p = pressure [Pa]
 q = heat flux [W/m^2]
 Q = preconditioned primitive variable
 r_{het} = heterogeneous reaction rate [$1/s$]
 R = radial direction distance [m]
 R_u = universal gas constant; $R_u = 8.134$ [$kJ/(kmol \cdot K)$]
 t = time [s]
 T = temperature [K]
 T_A = activation temperature [K]
 u = z velocity [m/s]
 $V_{chamber}$ = volume of catalyst bed chamber [m^3]
 v = r velocity [m/s]
 $W_{catalyst}$ = total mass of the catalyst pellets [kg]
 Y = mass fraction
 Z = axial direction distance [m]

Greek Symbols

α = axisymmetric coefficient
 Γ = preconditioning matrix
 ε = porosity of catalyst bed
 ε_p = particle void fraction
 ϕ_s = sphericity of catalyst pellet
 κ = turbulent kinetic energy [m^2/s^2]
 μ = viscosity [$kg/(m \cdot s)$]
 ρ = density [kg/m^3]
 τ = viscous stress tensor
 ω = specific dissipation rate [$1/s$]

Superscript

i = species index

Subscripts

0 = initial condition
 g = gas phase
 i = species index
 s = solid phase
 w = chamber wall

REFERENCES

- (1) Ley, W.; Wittmann, K.; Hallmann, W. *Handbook of Space Technology*; Wiley Press: New York, 2009.
- (2) Lee, S. T.; Lee, S. H.; Choi, Y. J.; Lew, J. H. Review on Monohydrazine Thruster Development. *J. Korea Soc. Propuls. Eng.* **1999**, *3* (3), 72–77.

- (3) Wucherer, E. J.; Cook, T.; Stiefel, M. Hydrazine Catalyst Production-Sustaining S-405 Technology. Presented at the 39th AIAA/ASME/SAE/ASEE Joint Propulsion Conference & Exhibit, Huntsville, AL, July 20–23, 2003; Paper No. AIAA-2003-5079.
- (4) Lee, K. H.; Yu, M. J.; Kim, S. K.; Jang, K. W.; Cho, S. J. Hot Firing Performance Measurement of Monopropellant Decomposition Catalyst and Domestic Development Status. *J. Korea Soc. Propuls. Eng.* **2006**, *10* (3), 109–117.
- (5) McRight, P.; Popp, C.; Pierce, C.; Turpin, A. Confidence Testing of Shell 405 and S-405 Catalysts in a Monopropellant Hydrazine Thruster. Presented at the 41th AIAA/ASME/SAE/ASEE Joint Propulsion Conference & Exhibit, Tucson, AZ, July 10–13, 2005; Paper No. AIAA-2005-3952.
- (6) Schmidt, E. W. *Hydrazine and Its Derivatives: Preparation, Properties, Applications*; Wiley–Interscience: New York, 2001.
- (7) Kesten, A. S. *Analytical Study of Catalytic Reactors for Hydrazine Decomposition*, Annual Progress Report No. F910461-12, NASA United Aircraft Research Laboratories, East Hartford, CT, 1967.
- (8) Crespo, A. *Steady State Analysis of Hydrazine Catalytic Thrusters for Different Types of Catalysts*; Instituto Nacional de Tecnica Aeroespacial “Esteban Terradas”: Madrid, Spain, 1976.
- (9) Shankar, V.; Ram, K. A.; Bhaskaran, K. A. Prediction of the Concentration of Hydrazine Decomposition Products along a Granular Catalytic Bed. *Acta Astronaut.* **1984**, *11* (6), 287–299.
- (10) Shankar, V.; Ram, K. A.; Bhaskaran, K. A. Experimental investigations of the 10 N catalytic hydrazine thruster. *Acta Astronaut.* **1985**, *12* (4), 237–249.
- (11) Makled, A. E.; Belal, H. Modeling of Hydrazine Decomposition for Monopropellant Thrusters. Presented at the 13th International Conference on Aerospace Sciences & Aviation Technology, 2009; No. ASAT-13-PP-22.
- (12) Kesten, A. S. *Analytical Study of Catalytic Reactors for Hydrazine Decomposition*, Quarterly Progress Report No. 6 G910461-21, United Aircraft Research Laboratories, East Hartford, CT, 1968.
- (13) Han, D. I.; Han, C. Y.; Shin, H. D. Empirical and Computational Performance Prediction for Monopropellant Hydrazine Thruster Employed for Satellite. *J. Spacecraft Rockets* **2009**, *46* (6), 1186–1195.
- (14) Jang, I. J.; Shin, H. S.; Shin, N. R.; Kim, S. H.; Kim, S. H.; Yu, M. J.; Cho, S. J. Macroporous-mesoporous alumina supported iridium catalyst for hydrazine decomposition. *Catal. Today* **2011**, DOI: 10.1016/j.cattod.2011.08.034.
- (15) Kim, S. K.; Lee, K. H.; Yu, M. J.; Cho, S. J.; Kim, I. T.; Lee, J. W. Life Verification and Qualification Test of Hydrazine Decomposition Catalyst for Monopropellant Thruster. In *Proceedings of KSAS 2009 Fall Conference*; Korean Society for Aeronautical & Space Science: Gyeongju, Korea, 2009; pp 521–524.
- (16) Schmitz, B. W.; Smith, W. W. *Development of Design and Scaling Criteria for Monopropellant Hydrazine Reactors Employing Shell 405 Spontaneous Catalyst*, Report No. RRC-66-R-76-Vol. II, Rocket Research Corporation, Redmond, WA, 1967.
- (17) Macdonald, I. F.; El-Sayed, M. S.; Mow, K.; Dullien, F. A. Flow Through Porous Media—The Ergun Equation Revisited. *Ind. Eng. Chem. Fundam.* **1979**, *18* (3), 199–208.
- (18) Weiss, J. M.; Smith, W. A. Preconditioning Applied to Variable and Constant Density Flows. *AIAA J.* **1995**, *33* (11), 2050–2057.
- (19) Shuen, J. S.; Chen, K. H.; Choi, Y. A Coupled Implicit Method for Chemical Non-Equilibrium Flows at All Speeds. *J. Comput. Phys.* **1993**, *106* (2), 306–318.
- (20) Liou, M. S. A Sequel to AUSM, Part II: AUSM⁺—Up for All Speeds. *J. Comput. Phys.* **2005**, *214*, 137–170.
- (21) Park, S. H.; Kwon, J. H. Implementation of k – w Turbulence Models in an Implicit Multigrid Method. *AIAA J.* **2004**, *42* (7), 1348–1357.
- (22) Smith, O. I.; Solomon, W. C. Kinetics of Hydrazine Decomposition on Iridium Surfaces. *Ind. Eng. Chem. Fundam.* **1982**, *21*, 374–378.
- (23) Kuo, K. *Principles of Combustion*; John Wiley & Sons: Hoboken, NJ, 2005.
- (24) Zehe, M. J.; Gordon, S.; McBride, B. J. CAP: A Computer Code for Generating Tabular Thermodynamic Functions from NASA Lewis Coefficient, NASA, Cleveland, OH, 2002; Report No. TP-2001-210959.
- (25) Daubert, T. E.; Danner, R. P. *Physical and Thermodynamic Properties of Pure Chemicals: Data Compilation*; Hemisphere Press: New York, 1989.
- (26) Kee, R. J.; Lewis, G. D.; Warantz, J.; Coltrin, M. E.; Miller, J. A.; Moffat, H. K. A Fortran Computer Code Package for the Evaluation of Gas-Phase, Multicomponent Transport Properties, Report No. SAND86-8246B, Sandia National Laboratories, Albuquerque, NM, 1998.
- (27) Cuffel, R. F.; Back, L. H.; Massier, P. F. Transonic Flow Field in a Supersonic Nozzle with Small Throat Radius of Curvature. *AIAA J.* **1969**, *7* (7), 1364–1366.
- (28) Lee, K. H.; Lee, S. N.; Yu, M. J.; Kim, S. K.; Baek, S. W. Combined Analysis of Thruster Plume Behavior in Rarefied Region by Preconditioned Navier-Stokes and DSMC Methods. *Trans. Jpn. Soc. Aeronaut. Space Sci.* **2009**, *52* (177), 135–143.